The case against gravitational millilensing in the multiply-imaged quasar B1152+199

Saghar Asadi,[1]⋆ Erik Zackrisson ,[2] Eskil Varenius ,[3,4] Emily Freeland,[1] John Conway[3] and Kaj Wiik[5]

[1]*Department of Astronomy, Stockholm University, Oscar Klein Center, AlbaNova, SE-106 91 Stockholm, Sweden*
[2]*Department of Physics and Astronomy, Uppsala University, Box 515, SE-751 20 Uppsala, Sweden*
[3]*Department of Earth and Space Sciences, Chalmers University of Technology, Onsala Space Observatory, SE-439 92 Onsala, Sweden*
[4]*Jodrell Bank Centre for Astrophysics, The University of Manchester, Oxford Rd, Manchester M13 9PL, UK*
[5]*Tuorla Observatory, Department of Physics and Astronomy, University of Turku, Väisäläntie 20, FI-215 00 Piikkiö, Finland*

ABSTRACT

Previous very long baseline interferometry (VLBI) observations of the quasar B1152+199 at 5 GHz has revealed two images of a strongly lensed jet with seemingly discordant morphologies. Whereas the jet appears straight in one of the images, the other exhibits slight curvature on milliarcsecond scales. This is unexpected from the lensing solution and has been interpreted as possible evidence for secondary, small-scale lensing (millilensing) by a compact object with a mass of 10^5–10^7 $M_\odot$ located close to the curved image. The probability for such a superposition is extremely low unless the millilens population has very high surface number density. Here, we revisit the case for millilensing in B1152+199 by combining new global–VLBI data at 8.4 GHz with two data sets from the European VLBI Network (EVN) at 5 GHz (archival), and the previously published 5 GHz Very Long Baseline Array (VLBA) data. We find that the new data with a more circular synthesized beam, exhibits no apparent milliarcsecond-scale curvature in image B. Various observations of the object spanning ∼15 yr apart enable us to improve the constraints on lens system to the point that the only plausible explanation left for the apparent curvature is the artefact due to the shape of the synthesized beam.

Key words: gravitational lensing: strong – galaxies: jets – dark matter.

1 INTRODUCTION

A generic prediction of the cold dark matter (CDM) model is the existence of dark halo substructure (a.k.a. subhaloes) in the mass range of dwarf galaxies and below. The mismatch between the observed luminosity function of satellite galaxies and the predicted mass function of dark matter haloes also implies that the vast majority of these substructures need to be extremely faint or completely dark at optical wavelengths. Pinning down the properties of this dark subhalo population provides an important test between CDM and alternative dark matter models which often predict subhaloes with significantly different mass functions and density profiles (e.g. Bose et al. 2016; Li et al. 2016)

Methods for hunting down dark matter subhaloes include the search for dark matter annihilation signals (e.g. Hütten et al. 2016; Mirabal et al. 2016; Schoonenberg et al. 2016), the perturbations of gas, stars, and stellar streams in the Milky Way (e.g. Chakrabarti

& Blitz 2011; Feldmann & Spolyar 2015; Carlberg 2016; Erkal et al. 2016), H I clouds with no stellar counterpart (e.g. Keenan et al. 2016) and effects of small-scale gravitational lensing. In the latter case, the main targets are distant galaxies and quasars that are strongly lensed by a foreground galaxy. By looking for small lensing perturbations introduced by substructure in the halo of the main lens, even completely dark subhaloes can in principle be detected (see Zackrisson & Riehm 2010, for a review). Using optical, near-infrared and sub-millimetre observations, this technique has already revealed various kind of lens substructure in the dwarf galaxy mass range (e.g. Vegetti, Czoske & Koopmans 2010; MacLeod et al. 2013; Nierenberg et al. 2014; Hezaveh et al. 2016; Inoue et al. 2016), and at least one strong case for a dark or extremely faint subhalo (Vegetti et al. 2012).

Very long baseline interferometry (VLBI) at radio or sub-mm wavelengths is currently the only technique that can detect such perturbations at milliarcseconds scale and below (e.g. Wilkinson et al. 2001; Fish et al. 2013; Zackrisson et al. 2013), but the small intrinsic sizes of the sources that are sufficiently bright for current observations of this type severely limits the categories

⋆ E-mail: saghar.asadi@astro.su.se

Table 1. Summary of the observational data sets considered for the B1152+199 core–jet system.

	VLBA	EVN 5 GHz	global VLBI
Project number	BB0133	EJ010	GA036
PI	Biggs	Jackson	Asadi
Epoch	Feb–Mar 2001	Mar 2012	June 2015
Observing frequency (GHz)	5	5	8.4
Beam size (mas)	3.3×1.6	2.3×1.8	1.2×0.5
Beam position angle (deg)	-9.2	0.4	-6.8
RMS noise (μJy beam^{-1})	63	17	26

of substructures that can be detected through such millilensing effects. Basically, only halo objects much denser than predicted in the standard cold dark matter scenario can be detected this way (Zackrisson et al. 2013) – like ultracompact minihaloes and primordial black holes.

Curiously, VLBI observations have already produced one tentative detection of gravitational millilensing – in the B1152+199 strong-lensing system, first identified by the Cosmic Lens All-Sky Survey (CLASS; Myers et al. 1999). In this case, a quasar at $z = 1.0189$ is lensed into two images A and B by a galaxy at $z = 0.4386$. VLBA observations by Rusin et al. (2002) have revealed that the two images, which are about 1.56 arcsec apart, exhibit a jet-core structure with a flux ratio of ~ 3:1. Optical observations by Toft, Hjorth & Burud (2000) indicate that image B – which is less magnified and passes closer to the lens galaxy – is subject to considerable dust attenuation, corresponding to a differential reddening of $E(B - V) \approx 1.0 \pm 0.1$ mag. The time delay between the images is estimated at $\approx$30–60 d (Toft et al. 2000; Edwards et al. 2001; Muñoz et al. 2001; Rusin et al. 2002).

As first noted by Rusin et al. (2002), the jet of image B exhibits a slight curvature on milliarcsecond scales that is not seen in the image A jet. They suggested substructure in the main lens galaxy to be a likely explanation of the curvature. The curvature was also interpreted by Metcalf (2002) as millilensing of an object of mass $\sim 10^5$–10^7 M$_\odot$ in the vicinity of image B. However, Metcalf (2002) also find that the type of substructure required to explain this feature would need to belong to a very numerous population of objects. Luminous objects in this mass range, like globular clusters and dwarf galaxies, fall short by a large factor. If the object is a dark matter halo or subhalo, it would also need to be far more compact than predicted by the standard CDM model.

Here, we present new and archival VLBI observations of the B1152+199 system to revisit the millilensing interpretation. The VLBI data are described in Section 2. The overall properties of the B1152+199 lensing system and our curvature analysis on image B is presented in Section 3. In Section 4, we present our hypothesis about the reason why previous VLBI map hinted at a curvature in image B. Finally, in Section 5, we summarize the findings of this study.

2 OBSERVATIONAL DATA

In this paper we analyse three VLBI observations of B1152+199, summarized in Table 1, including the 5 GHz VLBA data discussed by Rusin et al. (2002) and Metcalf (2002). All data sets were calibrated and imaged from the raw archival data using the same software – AIPS 31DEC15 (Greisen 2003) and PARSELTONGUE 2.3 (Kettenis et al. 2006) – to reduce systematics due to different

software and reduction strategies. In this section we describe the calibration and imaging of these three epochs.

2.1 BB0133: 5 GHz VLBA

The VLBA program BB0133 was observed on two days: 2001 February 27 and March 18. One single correlation centre was used between the two lensed images. These data were first presented in Rusin et al. (2002). Bandpass corrections were derived towards 3C279 and the visibility phases were referenced to J1148+1840, assuming a position from the RFC2016c calibrator catalogue at 1.9° separation from the target field. After transferring the cumulative corrections, the target was imaged. Prominent phase errors were detected, such as a double structure due to systematic phase-differences between the two observing days, even after phase-referencing. We cleaned the image assuming a clean box around the brightest peak in the A-image, and performed one round of phase-only self-calibration using the cleaned image as input model. A new image was made, and another round of self-calibration was performed, now solving also for amplitudes to adjust minor antenna offsets in particular at the start and end of the observing sessions. The corrections derived, once every minute, were inspected visually and found to vary slowly as expected. The cumulative corrections were applied to the target and the two lens images were imaged using Briggs (1995) weighting scheme with robustness parameter 0.5. We note that although the two observations in this experiment both used the same phase-reference calibrator, clear phase-errors were found towards the target after applying the calibrator solutions. Hence, although the relative antenna errors were corrected for by hybrid imaging of the target to provide phase coherence throughout the data, these data should not be used for absolute astrometry of the target field.

2.2 EJ010: 5 GHz EVN

The EVN program EJ010 was observed with 12 EVN telescopes and a single correlation centre was used between the two lensed images. Bandpass corrections were derived towards 3C345 and the visibility phases were referenced to J1143+1834 at 3.0° separation from the target field. After transferring the cumulative corrections the target was imaged. The target image was found to be dynamic-range limited due to phase errors. To correct these, multiple rounds of phase self-calibration were performed followed by one round of amplitude self-calibration. A box-cleaned phase-referenced image was used as starting model and solutions were found once per minute. Particular care was taken to antenna Sh which did not have enough signal to noise for reliable amplitude corrections to be found. The cumulative corrections were applied to the target and the two

lens images were imaged using Briggs (1995) weighting scheme with robustness parameter 0.5.

2.3 GA036: 8.4 GHz Global VLBI

The Global VLBI program GA036 was observed with 22 telescopes, including the VLBA, and used separate correlation centres for the two lens images. Bandpass corrections were derived towards J1224+2122 and the visibility phases were referenced to J1158+1821 at 1.5° separation from the target field. After transferring the cumulative corrections the target was imaged. The target image was found to be dynamic-range limited due to phase errors. To correct these, multiple rounds of phase-only self-calibration were performed (but no amplitude self-calibration) using a solution interval of 2 min. The brightest A-image was used to derive the corrections, using the phase-referenced image as starting model. The cumulative corrections were applied to both correlated data sets (e.g. both lens images). Both images were imaged using Briggs (1995) weighting scheme with robustness parameter 0.5. We note that although we did not manage to remove all residual phase errors from the B-image, we think that these data are the best for absolute astrometry as they have the smallest target-phase reference calibrator separation.

2.4 Images of the macrolensed jet

In Fig. 1, we present the contour maps of images A and B (lowest contour level is set to 3, 10, and 3 times the rms noise for the rows, respectively, from top to bottom and each level is a factor of $\sqrt{2}$ times the previous level) from the three data sets described in Sections 2.1, 2.2, and 2.3.

The apparent length of the jet is comparable in both 5 GHz data sets and in the 8.4 GHz set ($\approx$20 mas for image A and $\approx$8 mas for image B). While the jet in image A appears continuous in the VLBA 5 GHz data, it breaks up into separate blobs in the other data sets, likely due to combination of different image fidelity, sensitivity limits, and movement of blobs along the jet between the observation epochs. In agreement with Rusin et al. (2002), we find that image A appears straight with the best-fitting position angle varying no more than $\approx$ 1 deg between the data sets (see Table 2), once the small blob protruding from the core in the EVN 5 GHz map is ignored. This weak western blob extension could possibly be a hint of a counter-jet feature, but could also be an artefact due to e.g. phase residuals in the data. We ignore this feature in our analysis and focus on the clear eastern jet structure.

The flux ratios between the cores of images A and B are $\approx$3 to 1 in the two 5 GHz data sets, but closer to $\approx$4.5 to 1 in the 8.4 GHz data set. This is unexpected from a lensing point of view, since the flux ratio is set by the macrolens solution and is not expected to change over time scales of decades. However, the core of image A in the 8.4 GHz data set has double peaks, which may suggest that a very bright blob is currently emerging and therefore temporarily boosting the apparent flux of image A.

The position angle of image B is clearly different from the jet in image A, but this is – as explained in Section 3.1 – expected from the strong lensing (macrolensing) by the main lens galaxy. The tantalizing aspect of image B, on which the case for potential millilensing by a massive object in the vicinity of this object is based, is that in two out three data sets the jet exhibits slight downwards curvature – i.e. a trajectory that differs from a straight line. This curious feature is most clearly seen in the VLBA data set, and a hint of this is also present in the global VLBI maps, even though

it is – on its own – less convincing due to the gaps between the jet blobs.

It is perhaps worth keeping in mind that, as one can see in Fig. 1, if the EVN 5 GHz data had been observed first, the possibility of substructure lensing in the system would not have been discussed by Rusin et al. (2002) in the first place. This is especially curious once seen in light of a comparison between the shape of the synthesized beams and the fact that image B barely extends more than two beam sizes in length at 5 GHz (see Sections 4 and Fig. 4 for a discussion about this).

3 THE CASE FOR JET CURVATURE IN IMAGE B

3.1 The macrolens model

To investigate the expected shape of image B given a macrolens model without substructure, we use the GLAFIC lensing code (Oguri 2010) to model the B1152+199 main lens as a singular isothermal ellipsoid (SIE) with external shear. Given the goal of this modelling which is deriving the general direction of the jet in lensed images, and that the jet structure (especially in image B) seems to be mainly dominated by the shape of the synthesized beam, we work with a simplified source composed of multiple point sources. This also means that we do not need to solve the lens equation for the extended source structure, but only source positions. Constraints on the best-fitting solution are set by the observed core and jet positions of image A, the core of image B, the flux ratio between the images, the position of the centre of the SIE main lens, its position angle and ellipticity. The external shear in the software is described using six parameters; redshift, position (2), strength (γ), orientation (θ_γ), and the constant convergence(κ). It is reasonable to assume the redshift to be the same as that of the main lens.

We consider the centre of the external shear component to be forced to match the position of the main SIE. The model deals with the positional parameters of the external shear, and the convergence is assumed to be zero. In setting priors for the ellipticity and position angle of the main lens, we follow the general assumption that mass orientation follows light and therefore use the lens galaxy detected in Hubble Space Telescope (HST) *I*-band images as the reference. The fitting procedure is performed for each of the three data sets presented in Fig. 1 separately, but also for the combined map based on centring all maps on the core position of image A (see Table 2 for relative position measurements in this coordinate system).

Each set of data is run through the software with at least 3000 trials, and the combined data set is treated as a fourth data set. The uncertainties for each parameter derived using the 95 per cent inclusion range of values. These uncertainties are different for each data set. This is due to the various sizes of the synthesized beam (and therefore the uncertainties in jet position measurements), as well as number of jet blobs included in each data set. The numbers presented in Table 3 represent the maximum uncertainty in each parameter among the four mentioned data sets and fitting procedures.

Our fitting procedure differs in its assumptions from that carried out by Rusin et al. (2002) in the adopted main lens density profile. In their model, the second lens is to represent a possible satellite galaxy of the primary lens. This satellite galaxy (referred to as object X) is the explanation the authors use for an extended emission detected in the HST *I*-band image. They model the lens for the primary deflector (the main galaxy) to derive the power-law slope. They then add the potential galaxy X as the secondary deflector with the same mass
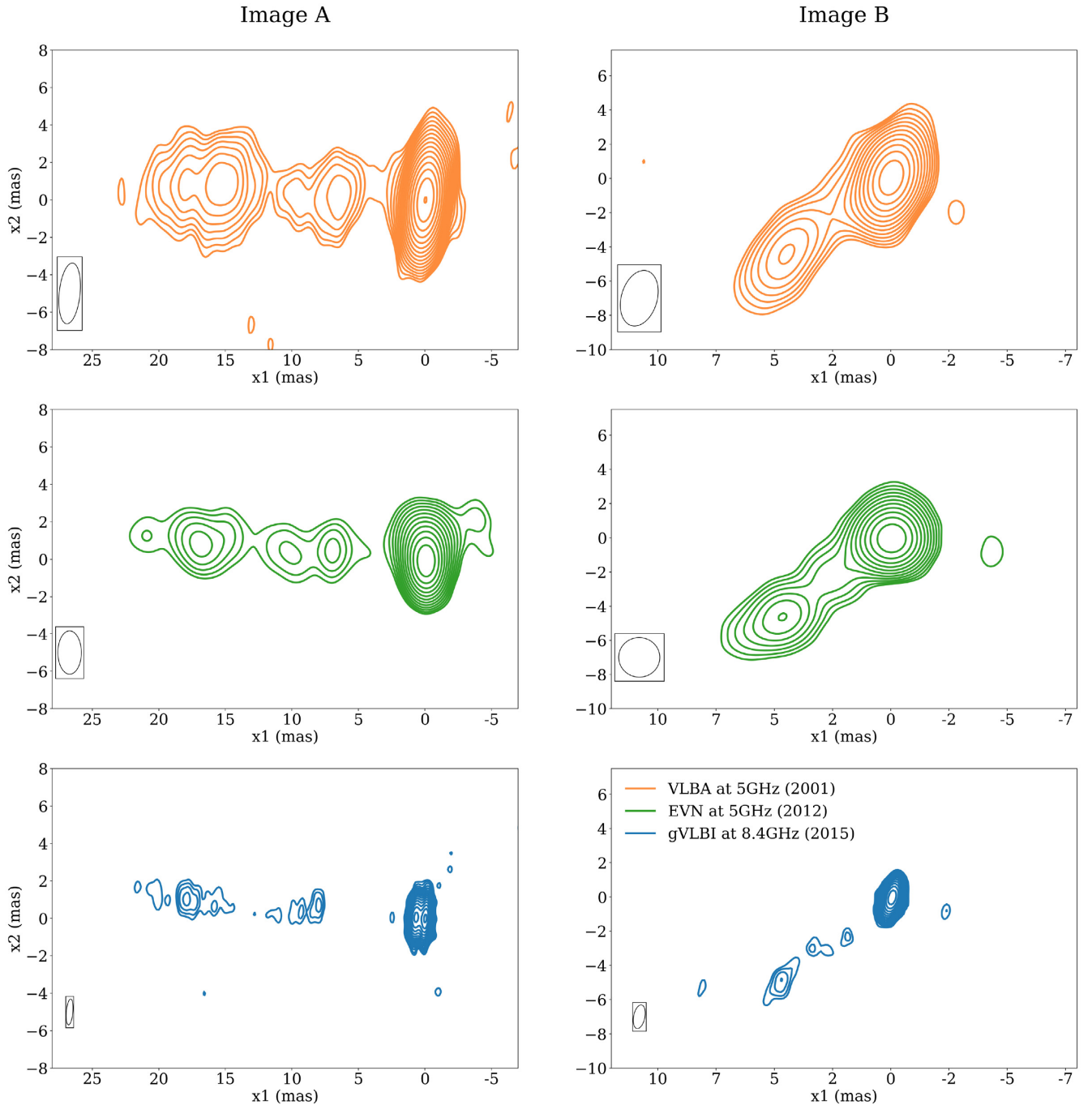
Figure 1. The two macrolensed images of B1152+199 from the re-imaged 1999 VLBA 5 GHz data set (top row), the 2012 EVN 5 GHz data set (middle row), and the 2015 Global VLBI array 8.4 GHz data set (bottom row). In each case, the beam size is indicated in the lower left corner. The faintest contours are set to 3, 10, and 3 times the rms noise, respectively, from top to bottom. Each subsequent contour is set at $\sqrt{2}$ times the previous one.

profile. The conclusion of this experiment done by Rusin et al. (2002) is that in order to reproduce the data, steeper mass profiles than isothermal are necessary for the system with both the primary and secondary lens. We have, on the other hand, fixed the main lens to be of SIE type and tried to model the data without including a secondary lens (the potential satellite galaxy or a dark substructure). In general, our inferred best-fitting lens parameters are similar to theirs. We have no problem reproducing the broad direction of this jet using a single lens only, as discussed in Section 3.2 and as shown on the image B in Fig. 2. This is most likely due to the additional

data sets with higher data quality, and to differences in how the position angle of the jet in image B is measured from the maps (not unambiguous, especially in the VLBA 5 GHz map, due to the apparent curvature).

3.2 Jet curvature

Macroimages that appear curved along the lens caustic are common in strong lensing situations where the source is an extended object. However, the very small apparent size of the image A jet ($\approx$20 mas)

Table 2. Measured coordinates in units of arcseconds for the core and jet (outermost blob) of B1152+199, setting A_{core} as the origin. Errors on all positions are ≈ 1 mas.

	VLBA (2001) $x_1\ x_2$	EVN (2012) $x_1\ x_2$	global VLBI (2015) $x_1\ x_2$
A_{jet}	0.0153+0.0011	0.0168+0.0009	0.0179+0.0099
B_{core}	0.9353−1.2454	0.9354−1.2455	0.9354−1.2455
B_{jet}	0.9308−1.2497	0.9310−1.2495	0.9306−1.2403

compared to the macrolens Einstein radius (≈ 0.75 arcsec) implies that very little curvature is expected due to the macrolens across the face of this image. Any observational hint of curvature in image A would correspond to intrinsic jet curvature in the source plane, and the apparent straightness of jet A therefore places a constraint on the intrinsic curvature of the jet. While the jet in image A appears fairly straight, the data quality also allows for slight upward curvature, which due to the reversed image parity between the images would translate into a downward curvature in image B. To evaluate the impact of any such potential curvature on the source plane on the observed images of the system, we performed an experiment. We assume two different structures for our source, and forward project it using the best-fitting lens model in Table 3. The two alternative sources are composed of (1) a core with a straight jet and (2) a core

with a jet with as much curvature as allowed by the faint end of the jet in image A, i.e. we fit a degree two polynomial to the recovered source positions. We then use the lens model in Table 3 to compare the lensed images of both sources with the observed maps of B1152 + 199. Fig. 3 depicts the result of this experiment. The orange line on each image depicts the trend an intrinsically straight source would follow at the position of each image given the macrolens model. The slightly curved green line is how the intrinsically curved source would be. The blue lines, shown for comparison, are derived from a deg-2 polynomial fit on the *image plane* to each image separately. The overlap of the blue and green lines on image A is expected, given how the curvature of the source is calculated. As one can see in both frames of Fig. 3, as far as the faintest contour plots of the observed maps (in image B) are concerned, the green and orange lines are overlapping and they only start deviating from each other at ∼7 mas away from the core. This also holds for the solid blue line in the right frame as well, while the dashed blue line that only includes the VLBA 5 GHz data starts deviating from the rest already at the centre of the jet in image B. One can interpret the blue lines as the position angle of image B as measured using the compound data set (the solid line), or the VLBA 5 GHz map only (dashed blue line).

In comparison to the analysis by Metcalf (2002), we find that our macrolens model provides a better fit to the overall direction of the jet in image B and can fully account for the observations (compare

Table 3. Best-fitting parameters for the macrolens model of B1152+199, using the combined measurements of all three data sets. The position offsets are measured with respect to the core of image A to be consistent with Table 2.

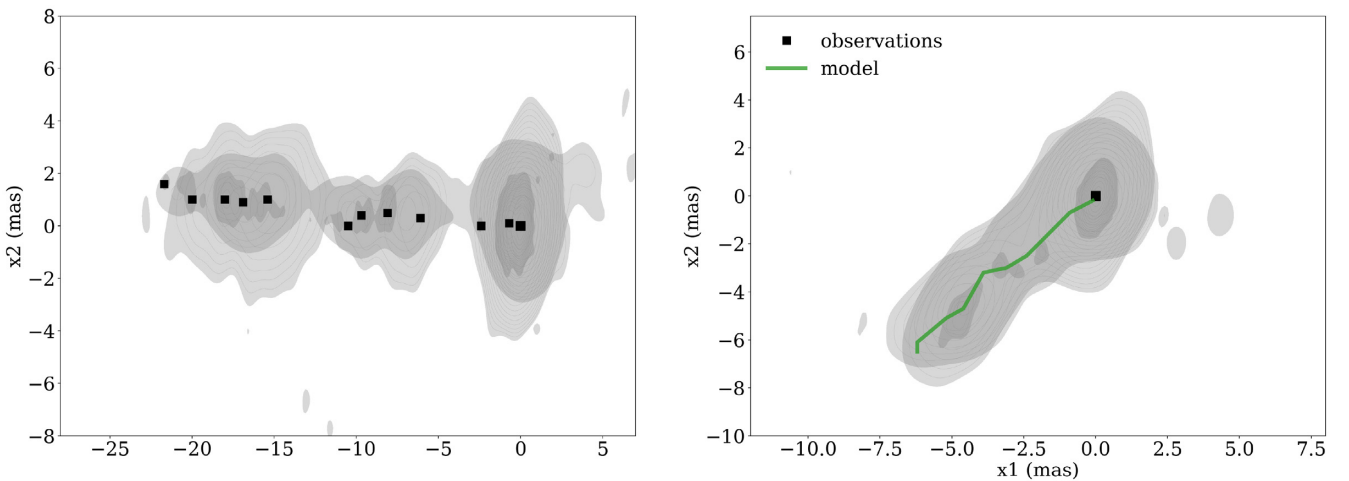| model				
SIE σ (km s^{-1})	**SIE x_1 (arcsec)**	**SIE x_2 (arcsec)**	**SIE e**	**SIE PA (deg)**
$2.46^{+0.04}_{-0.06} \times 10^2$	$0.55^{+0.04}_{-0.03}$	$-0.90^{+0.06}_{-0.03}$	$0.39^{+0.02}_{-0.02}$	-80^{+9}_{-12}
dt (days)	**shear x_1 (arcsec)**	**shear x_2 (arcsec)**	**shear γ**	**shear PA (deg)**
31^{+6}_{-5}	$0.55^{+0.03}_{-0.06}$	$-0.90^{+0.08}_{-0.04}$	$0.16^{+0.02}_{-0.09}$	-159^{+43}_{-23}
core x_1 (arcsec)	**core x_2 (arcsec)**	–	–	–
$0.37^{+0.04}_{-0.05}$	$-0.65^{+0.07}_{-0.08}$	–	–	–

Figure 2. Overlaid maps from the 5 GHz VLBA, 5 GHz EVN, and 8.4 GHz global VLBI observations of the two macrolensed images along with model fits (image A jet) and predictions (image B jet) assuming a macrolens with no substructure. The core positions of both images, and the brightest jet blobs of image A are used to constrain the model and predict the positions of the corresponding blobs in image B (under the assumption of no temporal evolution in the jet structure over the time-scale set by the ≈ 1 month time delay between the images). The green line depicts the predicted positions of the corresponding peaks (black squares) of image A, in image B.
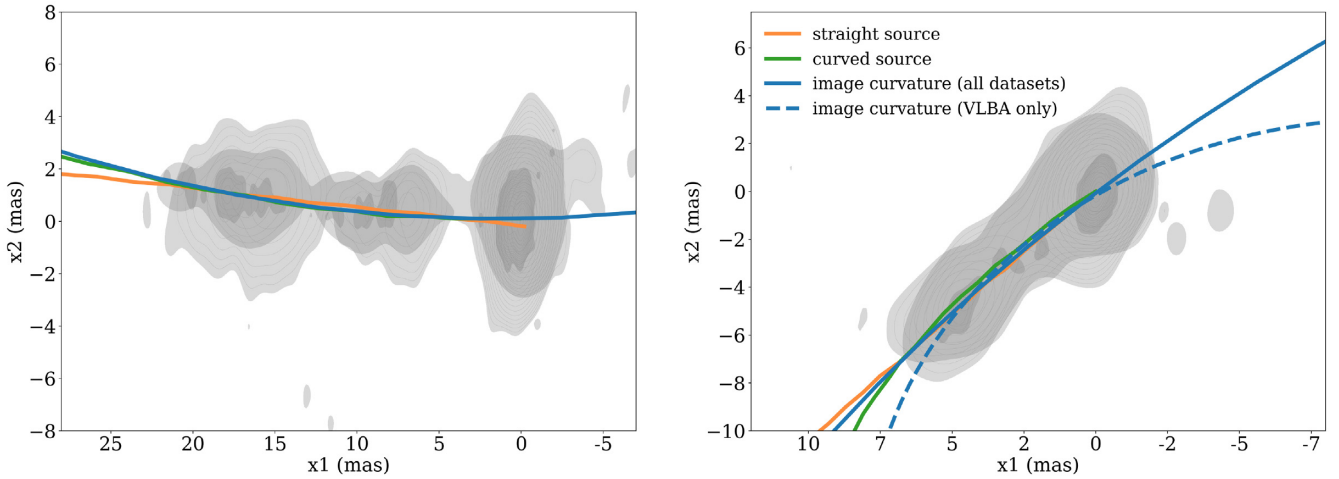
Figure 3. The experiment to test the result of internally straight versus curved source (on the source plane) on the observe lens images. The orange line assumes a straight source (on the *source plane* by fitting a straight line to the recovered point source positions) forward projected using our best-fitting model. The purpose of this line is to show the curvature at image B due to the main lens (no substructure). The green line assumes an intrinsically curved source (on the *source plane* by fitting a deg-2 polynomial to the recovered source blobs) forward projected using our best-fitting model. The purpose of this line is to show a comparison between the image B of an intrinsically curved jet with image B as observed. The blue lines are the result of a deg-2 polynomial fit on the *image plane* to each image separately, including the combined data set (solid line) and only the VLBA 5 GHz map (dashed line). The blue lines on image A and image B are independent from each other and from the smooth lens model. The purpose of these lines is the comparison between the apparent curvature on the image plane and the curvature on the source plane projected to the image plane by the lens model.

the solid and dashed blue lines to the model prediction, i.e. green line, in Fig. 3).

4 DISCUSSION

The combination of data sets presented here (spanning ∼15 yr in time), does not provide enough supporting evidence for any jet curvature in image B of B1152+199. We showed that our best-fitting models constrained by image A not only provide correct predictions on positions of corresponding blobs in image B, but also correctly reproduced the position angle of the jet (see Fig. 3). However, apparent small-scale curvature in the VLBA and gVLBI data sets (even though well within the uncertainty provided by the size of the beam) call for an explanation.

4.1 Beam effect

We believe that the most likely explanation for the apparent curvature in image B lies in the effect of the synthesized beam in the VLBA and gVLBI data sets. Given the elongated shape of the beam in the VLBA 5 GHz data and the gVLBI 8.4 GHz data, as opposed to the more circular beam in the EVN 5 GHz data, we performed an experiment in which we convolved both VLBA data to the same resolution. We used an elongated beam similar to the VLBA BB0133 programme (same orientation) but 30 per cent larger along both axes with the same position angle (Fig. 4). So, by convolving the EVN image with this beam we get an idea of how the EVN structure would look if observed with only the VLBA. Then, we convolve the EVN image to the same resolution. Convolving the VLBA image to this beam will only smooth the image marginally. Indeed, the convolved VLBA image shows the bending almost as clear as the original one. Overall, the convolved VLBA and convolved EVN images look very similar and exhibit slight apparent curvature among some of the contours. Based on this observations, we conclude that the bending is indeed a
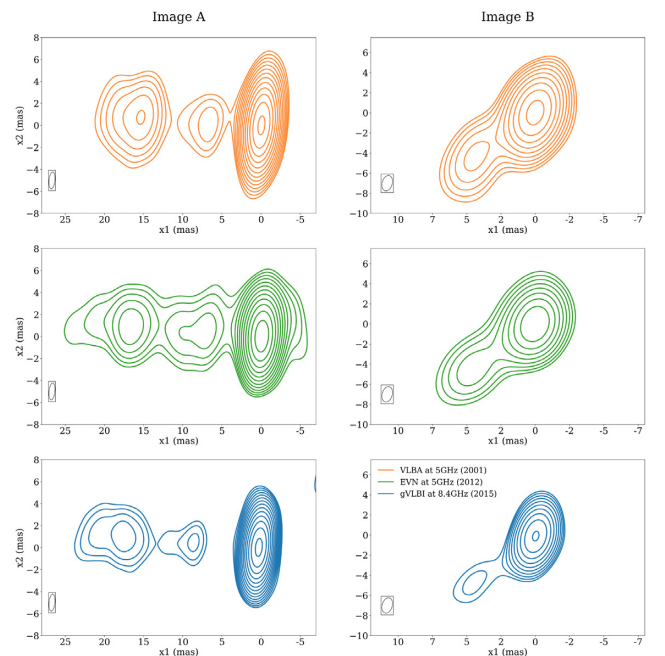

Figure 4. The experiment that shows the effect of beam size and ellipticity on the apparent curvature in image B. In this experiment, we convolve three data sets presented in Fig. 1 to the same beam to show the effect of beam ellipticity and position angle on the apparent curvature in image B.

convolution effect. As the EVN image at maximum resolution with a more circular beam shows no bending, and given that this data set is much more sensitive (more antennas etc.) than the VLBA one, this could explain the apparent curvature. For completeness, we also convolved the 8.4 GHz image of the B-image to the same resolution. Although slightly lower contours are used here since the signal is weaker, it again resembles well the other two convolved images.

This experiment suggests that the case for the curvature may be merely an effect of the elongated beam and even the best data set among those included in this study are unable to robustly determine that the jet in image B is curved.

5 CONCLUSIONS

Using new VLBI data at 5 GHz (EVN) and 8.4 GHz (global VLBI) together with the archival VLBA data, carefully re-calibrated and re-imaged, we have investigated the claimed case for curvature and gravitational millilensing in one of the images of the strongly lensed quasar jet B1152+199 that was previously discussed by Rusin et al. (2002) and Metcalf (2002). Through the analysis presented in this study, we refute the presence of previously claimed curvature in image B within the size of the smallest synthesized beam. Hence, we find no need for an additional secondary lens, and argue that the apparent curvature could be explained as a mere artefact of the synthesized beam.

ACKNOWLEDGEMENTS

REFERENCES

Bose S., Hellwing W. A., Frenk C. S., Jenkins A., Lovell M. R., Helly J. C., Li B., Gao L., 2017, MNRAS, 464, 4520
Briggs D. S., 1995, PhD thesis, The New Mexico Institute of Mining and Technology
Carlberg R. G., 2016, ApJ, 820, 45
Chakrabarti S., Blitz L., 2011, ApJ, 731, 40
Edwards P. G., Lovell J. E. J., Hirabayashi H., Jauncey D. L., Toft S., 2001, Publ. Astron. Soc. Aust., 18, 172
Erkal D., Belokurov V., Bovy J., Sanders J. L., 2016, MNRAS, 463, 102
Feldmann R., Spolyar D., 2015, MNRAS, 446, 1000
Fish V. et al., 2013, preprint (arXiv:1309.3519)
Greisen E. W., 2003, in Heck A., ed., Information Handling in Astronomy – Historical Vistas, Vol. 285. Kluwer Academic Publishers, Dordrecht, 109.
Hezaveh Y. D. et al., 2016, ApJ, 823, 37
Hütten M., Combet C., Maier G., Maurin D., 2016, J. Cosmol. Astropart. Phys., 2016, 47
Inoue K. T., Minezaki T., Matsushita S., Chiba M., 2016, MNRAS, 457, 2936
Keenan O. C., Davies J. I., Taylor R., Minchin R. F., 2016, MNRAS, 456, 951
Kettenis M., van Langevelde H. J., Reynolds C., Cotton B., 2006, in Gabriel C., Arviset C., Ponz D., Enrique S., eds, ASP Conf. Ser. Vol. 351, Astronomical Data Analysis Software and Systems XV. Astron. Soc. Pac., San Francisco, p. 497
Li R., Frenk C. S., Cole S., Gao L., Bose S., Hellwing W. A., 2016, MNRAS, 460, 363
MacLeod C. L., Jones R., Agol E., Kochanek C. S., 2013, ApJ, 773, 35
Metcalf R. B., 2002, ApJ, 580, 696
Mirabal N., Charles E., Ferrara E. C., Gonthier P. L., Harding A. K., Sánchez-Conde M. A., Thompson D. J., 2016, ApJ, 825, 69
Muñoz J. A. et al., 2001, ApJ, 563, L107
Myers S. T. et al., 1999, AJ, 117, 2565
Nierenberg A. M., Treu T., Wright S. A., Fassnacht C. D., Auger M. W., 2014, MNRAS, 442, 2434
Oguri M., 2010, PASJ, 62, 1017
Rusin D., Norbury M., Biggs A. D., Marlow D. R., Jackson N. J., Browne I. W. A., Wilkinson P. N., Myers S. T., 2002, MNRAS, 330, 205
Schoonenberg D., Gaskins J., Bertone G., Diemand J., 2016, J. Cosmol. Astropart. Phys., 5, 028
Toft S., Hjorth J., Burud I., 2000, A&A, 357, 115
Vegetti S., Czoske O., Koopmans L. V. E., 2010, MNRAS, 407, 225
Vegetti S., Lagattuta D. J., McKean J. P., Auger M. W., Fassnacht C. D., Koopmans L. V. E., 2012, Nature, 481, 341
Wilkinson P. N. et al., 2001, Phys. Rev. Lett., 86, 584
Zackrisson E., Riehm T., 2010, Adv. Astron., 2010, 478910
Zackrisson E. et al., 2013, MNRAS, 431, 2172

This paper has been typeset from a T_EX/L^AT_EX file prepared by the author.